Geophysical Research Letters

RESEARCH LETTER
10.1029/2020GL090763

Key Points:

- Simulate magnetospheric-ionospheric particle interactions in martian crustal cusps with kinetic, 1.5-dimensional particle-in-cell model
- Crustal magnetic field strengths between 20 and 160 nT lead to increased field-aligned potentials with upward pointing electric fields
- Net ionospheric ion outflow from cusps increases more than a factor of two in the case with strongest crustal fields of 160 nT

Correspondence to:
A. R. Poppe,
poppe@ssl.berkeley.edu

Citation:
Poppe, A. R., Brain, D. A., Dong, Y., Xu, S., & Jarvinen, R. (2021). Particle-in-cell modeling of Martian magnetic cusps and their role in enhancing nightside ionospheric ion escape. *Geophysical Research Letters*, *48*, e2020GL090763. https://doi.org/10.1029/2020GL090763

Received 9 SEP 2020
Accepted 30 NOV 2020

© 2020. American Geophysical Union. All Rights Reserved.

Particle-In-Cell Modeling of Martian Magnetic Cusps and Their Role in Enhancing Nightside Ionospheric Ion Escape

A. R. Poppe[1], D. A. Brain[2,3], Y. Dong[3], S. Xu[1], and R. Jarvinen[4,5]

[1]Space Sciences Laboratory, University of California at Berkeley, Berkeley, CA, USA, [2]Department of Astrophysical and Planetary Sciences, University of Colorado at Boulder, Boulder, CO, USA, [3]Laboratory for Atmospheric and Space Physics, University of Colorado at Boulder, Boulder, CO, USA, [4]Department of Electronics and Nanoengineering, School of Electrical Engineering, Aalto University, Espoo, Finland, [5]Finnish Meteorological Institute, Helsinki, Finland

Abstract Amongst various escape channels, ion outflow is a major contributor to atmospheric loss at Mars over geologic time. On Mars' nightside, observations have indicated that cusp regions within crustal magnetic fields are associated with phenomena such as accelerated particle populations, discrete auroral emissions, and ionospheric outflow; however, the kinetic physics occurring within crustal magnetic cusps is poorly understood. Here, we present 1.5-dimensional particle-in-cell simulations of magnetospheric-ionospheric interactions within martian crustal magnetic cusp regions of varying strength. Simulation results demonstrate the formation of quasi-static, field-aligned potentials pointing away from Mars that accelerate electrons into the martian atmosphere while accelerating ions away, thereby enhancing ionospheric escape. Escaping ionospheric flux scales with crustal field strength, with 160 nT crustal fields yielding >2× the ion escape flux than in the case with no crustal fields. We discuss these results and conclude that magnetic cusp regions may be significant sources of ion loss at Mars.

Plain Language Summary Over 4.5 billion years, Mars' atmosphere has gone from warm and dense to cold and thin. An enduring scientific question is how and why Mars lost nearly its entire atmosphere. One possible mechanism for atmospheric loss at Mars is ionospheric escape. Neutral atoms in Mars atmosphere become ionized by gaining a charge after which they are subject to strong electromagnetic forces, which may be sufficient to overcome Mars' gravity and allow the ion to escape Mars completely. Here, we examine a particular environment at Mars, namely, regions on the nightside of Mars that possess strong crustal magnetic fields that are "open," meaning one end of the field line connects to Mars while the other is open to space. We use a "particle-in-cell" model that tracks the behavior of individual ions and electrons as they interact with both magnetic and electric fields. Overall, the model predicts that in regions of strong open crustal magnetic fields, electromagnetic forces stimulate excess ionospheric escape, more than twice the escape in cases with no crustal magnetic fields. These findings are significant as they suggest that regions of open magnetic fields may have contributed significantly to the loss of Mars' atmosphere over geologic time.

1. Introduction

Over its ~4.5 billion years history, Mars has lost its atmosphere. While there exists a preponderance of evidence that the early martian climate was warm and wet, with relatively high global atmospheric pressures (e.g., Davis et al., 2016; Owen, 1992; Poulet et al., 2005), Mars today is cold and dry, with a thin global CO_2 atmosphere of <~10 mbar of pressure (Hess et al., 1979). Thus, an enduring scientific question remains: namely, how, why, and when did Mars lose its atmosphere? Sequestration of atmospheric carbon into the surface and subsurface of Mars is one postulated pathway, yet evidence suggests that there is an insufficient amount of carbon in the present-day surface of Mars to account for the expected atmospheric loss (e.g., Bibring et al., 2005; Edwards & Ehlmann, 2015). Atmospheric escape to space is the other main loss pathway and manifests itself in a variety of processes, including Jeans escape (e.g., Tian et al., 2009; Walterscheid et al., 2013), photochemical escape via dissociative recombination (e.g., Cui et al., 2019; Fox & Hać, 2009; Lillis et al., 2017), neutral knock-on sputtering (e.g., Jakosky et al., 1994; Leblanc & Johnson, 2001; Luhmann et al., 1992), and acceleration of ionospheric species away from the planet via electric fields (e.g.,

Brain et al., 2015; Carlsson et al., 2006; Cravens et al., 2002; Dong et al., 2015; Dubinin et al., 2011). Recent observations by NASA's Mars Atmospheric and Volatile EvolutioN (MAVEN) mission have concluded that the sum of these loss-to-space processes can account for nearly 1 bar of atmospheric CO_2 pressure, thereby representing a significant, if not dominant, source of atmospheric loss (Jakosky et al., 2018). In turn, understanding the atmospheric loss mechanisms at Mars has far-reaching implications for the habitability of worlds in our solar system and in exoplanetary systems (e.g., Airapetian et al., 2017; Dong et al., 2017, 2018; Seager, 2013).

As the primary source of atmospheric ions, the martian ionosphere plays an important role in mediating the loss of both neutral and ionized material to space. On Mars' nightside, the ionosphere is controlled by processes such as neutral atmospheric dynamics, day-to-night bulk plasma transport, meteoritic ablation and ion deposition (e.g., Haider et al., 2013; Withers et al., 2008), solar energetic particle deposition (e.g., Girazian et al., 2017a), crustal magnetic field topology, suprathermal electron precipitation (e.g., Adams et al., 2018; Akbari et al., 2019; Brain et al., 2006; Girazian et al., 2017b; Lillis et al., 2009), and field-aligned potentials from ambipolar ionospheric expansion (e.g., Dubinin et al., 2008a; Xu et al., 2018). While unmagnetized to first-order, Mars possesses remanent crustal magnetic fields distributed in-homogeneously over the surface that are known to significantly alter its interaction with the solar wind and space plasma environment. In particular, the cusp regions of crustal magnetic fields, where field lines on the nightside are most likely to be open to the martian magnetotail, are associated with a plethora of physical processes due to the exchange of charged particles between the ionosphere and magnetosphere. These processes include discrete UV auroral emission (e.g., Bertaux et al., 2005; Gérard et al., 2015; Leblanc et al., 2006), electron precipitation into the nightside atmosphere (e.g., Brain et al., 2006; Lundin et al., 2006a; Bisikalo et al., 2017), and small-scale horizontal perturbations to the magnetic field (e.g., Brain et al., 2006). Associated phenomena include enhanced ionization signatures (e.g., Safaeinili et al., 2007; Němec et al., 2011) and escaping ionospheric ions (e.g., Lundin et al., 2006b; Dubinin et al., 2020). It seems plausible that magnetospheric-ionospheric coupling within martian magnetic cusps is a root driver of much of the above phenomena, in analogy to similar processes that are known to operate in the terrestrial magnetospheric cusp and polar regions (e.g., Reiff et al., 1988; Schriver & Ashour-Abdalla, 1993; André & Yau, 1997; Schriver, 1999).

Despite these observations associating martian crustal magnetic fields with various phenomena, we still do not fully understand the kinetic physics present within martian magnetic crustal cusp regions. While there have been a plethora of modeling-based studies of the martian magnetosphere in a global sense (e.g., Ma et al., 2004; Dubinin et al., 2008b; Brain et al., 2010; Dong et al., 2014; Holmström & Wang, 2015; Brecht et al., 2016; Jarvinen et al., 2016, 2018; Ledvina et al., 2017; Egan et al., 2018) and in particular, the role of crustal magnetic fields in altering global martian ion escape (e.g., Fang et al., 2010, 2015; Brecht & Ledvina, 2014; Romanelli et al., 2018), there has been to date no *fully kinetic* model of the magnetospheric-ionospheric interaction within a crustal magnetic cusp region that can resolve both ion and electron physics. Here, we present 1.5-dimensional particle-in-cell (PIC) modeling results of the ionospheric-magnetospheric plasma interaction along a crustal magnetic field cusp connected to the martian nightside ionosphere. In particular, these simulations are designed to quantify the formation of field-aligned electrostatic potential drops within magnetic cusps formed by differential penetration of magnetospheric ions and electrons and the effects of these field-aligned potentials on martian ionospheric ion escape. In Section 2, we describe the PIC model including its basic principles, operations, and assumptions. In Section 3, we present the results of the PIC simulations focusing on the dependence of the results on changes in the strength of the martian crustal magnetic field magnitude. Finally, in Section 4, we discuss the results and conclude.

2. Model Description

We have used a 1.5-dimensional particle-in-cell (PIC) code to model the kinetic interaction of magnetospheric and ionospheric plasmas in the martian nightside ionosphere, adapted from a similar (albeit simpler) 1.5-d PIC model previously used to investigate the solar wind interaction with lunar crustal anomaly cusps (Poppe et al., 2012). The 1.5-d PIC model traces both particle ions and electrons along a single spatial dimension and in two velocity dimensions, see cartoon in Figure 1a. By virtue of having a single spatial dimension, the modeled magnetic topology is restricted to following a single field line that is open to the

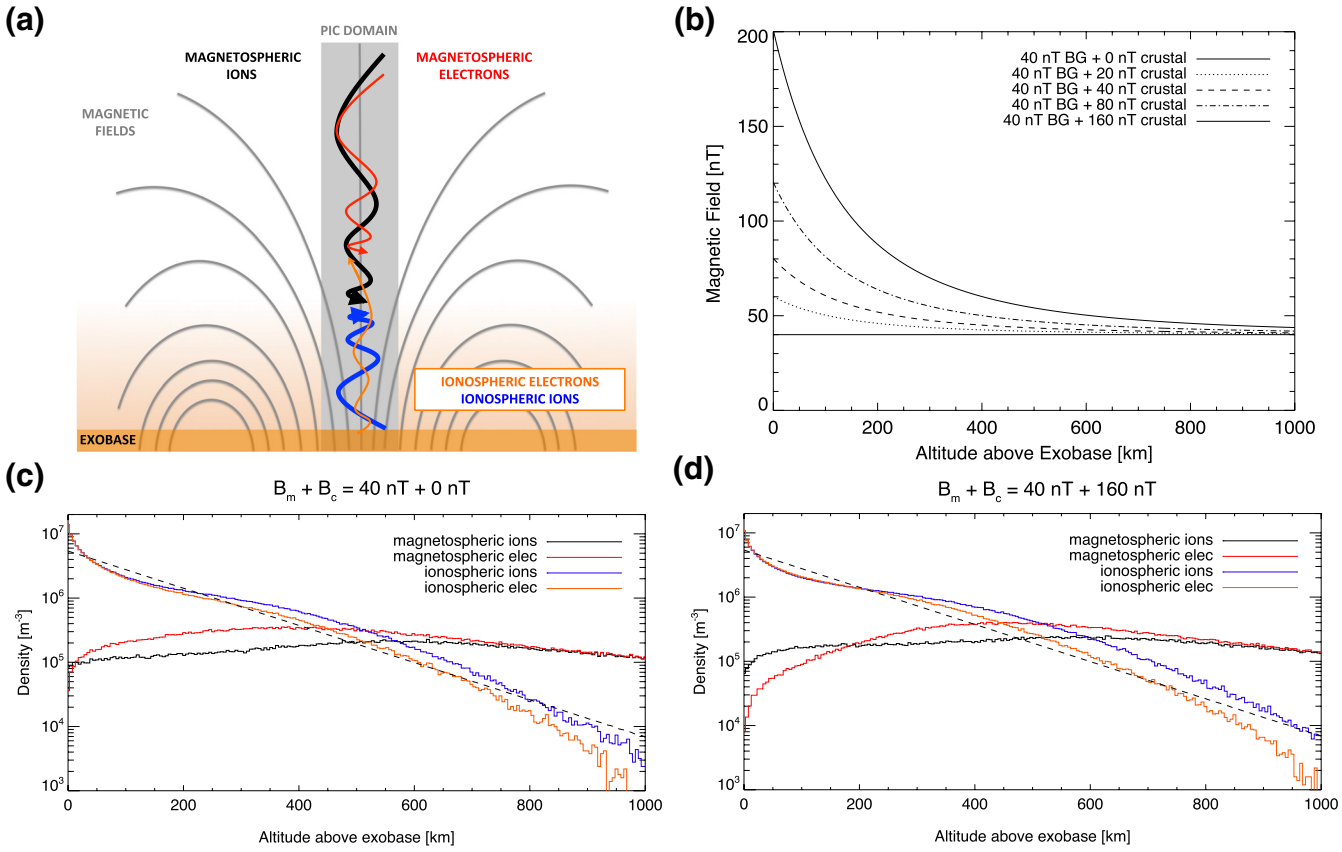

Figure 1. (a) A cartoon of the martian crustal magnetic cusp region, including magnetic fields, the four simulated particle species, and the PIC domain region along a single field line. (b) The magnetic field magnitude vs. altitude above the nightside exobase. All simulations have a spatially constant 40 nT magnetospheric field plus varying levels of dipolar, crustal magnetic field strengths. (c) and (d) The particle densities as a function of height above the exobase for the $B_c = 0$ nT case and the $B_c = 160$ nT case, respectively. The black dashed line in both panels denotes the initially preloaded ionospheric ion and electron density.

nightside martian ionosphere, i.e., the lower end point of the field line connects to the martian ionosphere and the upper end point is open to the downstream martian magnetosphere. The magnetic field is preset in the simulation and remains constant, as this study focuses on electrostatic phenomena as opposed to fully electromagnetic phenomena. Simulations of more complex magnetic topologies are beyond the scope of the current study, as they would require higher-dimensionality models (e.g., Fang et al., 2015; Romanelli et al., 2018). The two velocity dimensions track particle velocities parallel and perpendicular to the magnetic field line, respectively, with positive parallel velocities directed away from Mars. Parallel velocities are dynamically calculated according to local electrostatic fields, the magnetic mirror force, and gravity, while the perpendicular velocity is updated via a simple analytic expression, assuming conservation of the first adiabatic invariant for all particles ($\mu = mv_\perp^2 / 2B$). As is standard in PIC codes (e.g., Birdsall & Langdon, 1985), the electrostatic field is determined by first calculating the charge density on a spatially discretized grid, then calculating the electrostatic potential, ϕ, via Poisson's equation, and finally by interpolating $E = -\nabla\phi$ to the particle positions. For the gravitational force, we use an artificially large mass for Mars to ensure that the heavy ionospheric ions are gravitationally bound (i.e., the thermal ion velocity is approximately less than the gravitational escape velocity), given the relatively light mass for heavy ions used in the PIC model, as described below. We note that this 1.5-d PIC model for the martian nightside ionosphere shares many similarities with previous 1.5-d PIC simulations of the terrestrial auroral zone (e.g., Schriver & Ashour-Abdalla, 1993; Schriver, 1999).

The PIC model domain extends ~1,000 km tailwards from the martian nightside exobase, which we take to be at an altitude of 250 km above the martian surface. The PIC model uses a variable grid spacing throughout

such that the local Debye length at any point in the simulation is resolved by at least a factor of two. At the lower boundary, the Debye length is on the order of ~3 m while at the upper boundary, the Debye length is ~160 m (see discussion of particle parameters below). We used a time step of, $\delta t = 0.1\omega_{pe}^{-1} \approx 1.0$ μsec, where ω_{pe} is the highest plasma frequency expected in the model. Each simulation was run for 10 s and particle and field quantities were periodically printed out. The results were confirmed to have achieved a steady-state equilibrium before terminating the simulation.

The PIC model includes two sources of magnetic fields: magnetospheric fields, B_m, and crustal magnetic fields, B_c. For all simulations, the magnetospheric field is set to a spatially constant $B_m = 40$ nT, which is somewhat higher in magnitude than typically observed at the near-martian nightside; however, a stronger background field allows us to keep the domain smaller by ensuring that the magnetic field at the upper boundary is predominantly background field. The crustal magnetic field is modeled as dipole source buried in the martian crust, oriented such that the cusp field line is parallel with the magnetospheric field and thus, the two magnetic fields add constructively. The crustal field dipoles are placed at ~150-km depth below the martian surface, slightly deeper than—but nevertheless on the order of—previous estimations for magnetic sources (e.g., Nimmo & Gilmore, 2001; Voorhies, 2008). The primary external variable of interest in our simulations is the strength of the crustal magnetic field. Thus, we ran five simulations with crustal magnetic field strengths at the lower simulation boundary of $B_c = 0$, 20, 40, 80, and 160 nT, respectively, and kept all other simulation variables identical. The first of these simulations, with no crustal field contribution (and thus, a constant $B_m = 40$ nT field throughout the domain), serves as a "control" simulation to quantify the strength of ambipolar field-aligned potentials expected to be generated from polar-wind type outflows, as seen both at Earth and Mars (e.g., Collinson et al., 2015; Dubinin et al., 2008a; Xu et al., 2018). The following four simulations increase the crustal magnetic field strengths by factors of 2, starting at 20 nT (for a total field strength at the exobase of $B_m + B_c = 40 + 20$ nT = 60 nT), up to 160 nT (for a total field strength at the exobase of 200 nT). Figure 1b shows the magnetic field magnitude vs. altitude above the exobase for all five simulations. When compared to the control simulation with no crustal magnetic field, these simulations quantify the strength of additional field-aligned potentials generated from differential penetration of magnetospheric ions and electrons into the martian crustal magnetic cusp region.

The magnetospheric plasma consists of ions and electrons, injected at the upper boundary as drifting Maxwellians with a drift velocity of −250 km/s marsward, isotropic temperatures of $T_i = T_e = 50$ eV, and density of 0.1 cm^{-3}. The magnetospheric ion to electron mass ratio was set to $m_i/m_e = 1{,}600$, very close to the physical value for protons ($m_p/m_e \approx 1{,}836$). The marsward velocity of the magnetospheric plasma is higher than observed in the martian magnetotail (e.g., ~50 km/s as reported by Harada et al., 2015); however, a higher inflow velocity allows the model to obtain equilibrium faster. The ionospheric plasma consists of "heavy ions" and electrons, preloaded into the simulation at time, $t = 0$. The initial ionospheric plasma has zero drift velocity, temperature, $T_{ii} = T_{ie} = 1$ eV (where the subscripts *ii* and *ie* refer to "ionospheric ions" and "ionospheric electrons," respectively), and a density profile with an exponential scale of $H = 175$ km. The density at the lower boundary (i.e., the exobase) is set to be 5 cm^{-3}. With this exobase density and scale height, the initial density of ionospheric species at the upper boundary of the simulation domain (~1,000 km above the exobase) is ~0.005 cm^{-3}, a factor of ~20 less than the incoming magnetospheric plasma. The ionospheric ion to electron mass ratio was set to, $m_{ii}/m_e = 3{,}200$. We note that this ionospheric ion mass is much less than occurs physically, where the dominant nightside ion is O_2^+ ($m_{O_2} / m_e \approx 59{,}000$) (e.g., Girazian et al., 2017a; Wu et al., 2019); however, such an approximation is necessary and standard practice for PIC models to achieve computational closure.

At the upper boundary, magnetospheric particles are continuously injected per the prescribed initial conditions while any particles that reach the upper boundary with positive velocity are removed from the simulation. We assume particles that cross the upper boundary to be "lost" to the magnetotail. At the lower boundary, any particles (ionospheric or magnetospheric) that cross the boundary with downwards velocity are immediately reintroduced into the simulation at the lower boundary with velocities taken from the cold ionospheric distribution. This choice essentially assumes that any particle that crosses the exobase will eventually become thermalized to the cold, background ionospheric plasma. We note that we do not include either energy-dependent electron impact ionization of martian neutrals (e.g., Haider et al., 1992; Lillis et al., 2009, 2011, 2018) or ion-electron recombination in this version of the model (although both effects

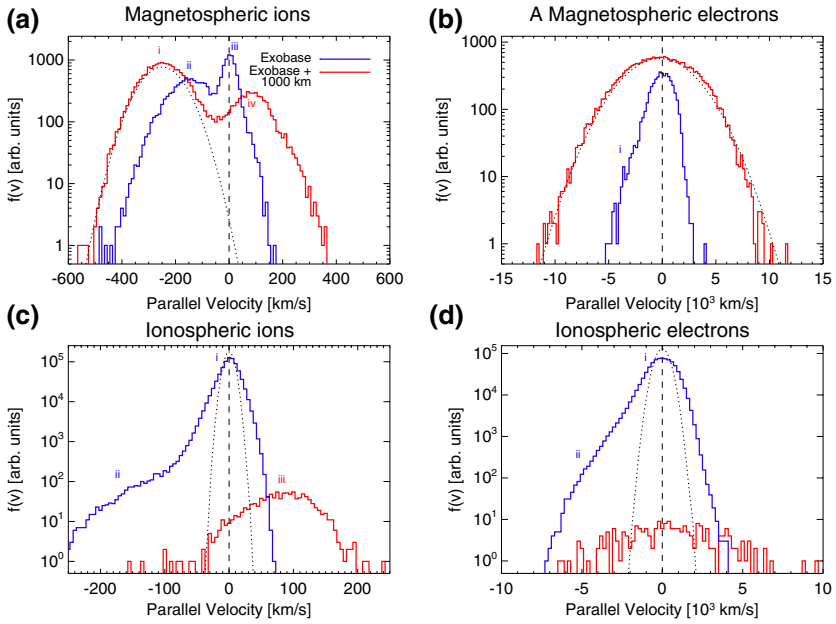

Figure 2. The parallel velocity distributions for the $B_m + B_c = 40$ nT + 160 nT case, including (a) magnetospheric ions, (b) magnetospheric electrons, (c) ionospheric ions, and (d) ionospheric electrons at the lower boundary ("exobase"; blue) and the upper boundary ("exobase + 1,000 km"; red). Dotted black curves are the initial or injected distributions for each species, respectively. Particular features of note discussed in the text are labeled with lowercase Roman numerals (e.g., i, ii, ...).

can be plausibly added in future studies). Thus, we are not self-consistently "generating" the nightside ionosphere, but rather presupposing its existence and focusing instead on its interaction with crustal fields and precipitating magnetospheric plasma.

3. Model Results

Panels 1c and 1d show the final particle densities at the end of the simulation time for all four species as a function of altitude above the exobase for the $B_m + B_c = 40$ nT + 0 nT case and the $B_m + B_c = 40$ nT + 160 nT case, respectively. Note that while not easily discernible from panels 1c and 1d, the plasma is quasi-neutral throughout the domain to values on the order of 10^{-2} to 10^{-4}. In both panels, the black dashed line denotes the *initial* density profile for both ionospheric ions and electrons, namely a exponential distribution with a scale height of 150 km and exobase density of 5×10^6 m^{-3}. In both cases, the magnetospheric ion and electron species (black and red curves, respectively) penetrate through the domain down to the lower boundary of the model at the exobase. The ionospheric ion and electron densities (blue and orange, respectively) deviate slightly from their original distribution. The increase in ionospheric densities at the lowest altitudes (>∼50 km above the exobase) is due to the reemission of magnetospheric particles as ionospheric particles. By comparing the case without a crustal field, panel 1c, to the case with 160 nT crustal field, panel 1d, one can see several differences including decreased magnetospheric electron densities especially in the lower 200 km of the simulation and increased densities of ionospheric ions especially above ∼800 km above the exobase. The presence of the strong crustal magnetic field in the latter case causes magnetospheric electrons to mirror above the exobase, thus decreasing their density at low altitude. The differential penetration of magnetospheric ions and electrons also stimulates the formation of increased field-aligned potentials, which contribute to increased densities of outflowing ionospheric ions at high altitudes.

Figure 2 shows the parallel velocity distributions at the end of the simulation time period for (a) magnetospheric ions, (b) magnetospheric electrons, (c) ionospheric ions, and (d) ionospheric electrons, at both the lower boundary ("exobase"; blue curves) and upper boundary ("exobase + 1,000 km"; red curves), respectively, for the run with $B_c = 160$ nT. Additionally, for comparison, each panel shows the initial or injected

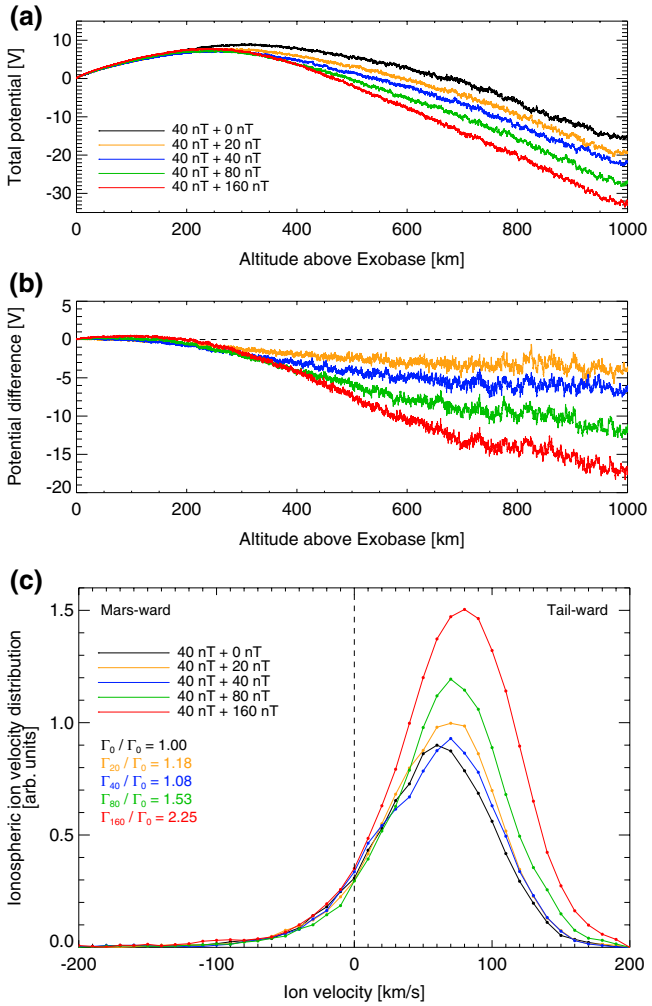

Figure 3. The (a) total potential for all cases and (b) difference in potential between the four cases with crustal magnetic fields (B_c = 20 nT, 40 nT, 80 nT, and 160 nT, respectively) and the B_c = 0 case, as a function of altitude above the exobase. (c) The ionospheric ion velocity distribution at the upper simulation boundary (z = exobase + 1,000 km) for all five simulations. The ratios of the total tailward ionospheric ion flux, Γ, for all five cases to the B_c = 0 nT case are listed as an inset.

parallel velocity distribution as dotted black curves. These distributions reveal much of the behavior of the particles as they interact with the crustal magnetic field and parallel electric fields. In panel 2a, the magnetospheric ions at both the upper and lower boundaries show double-peaked distributions. The upper distribution labeled "i" is the injection of fresh magnetospheric ions with a marsward drift of −250 km/s. Upon transiting through the entire simulation domain to the exobase, labeled "ii," the magnetospheric ions have been slowed to a bulk speed of ∼150 km/s and reduced in number via both magnetic mirroring and electrostatic deceleration (see discussion of field-aligned potentials below). The magnetospheric ion distribution at the exobase has a second peak, labeled "iii," centered at zero net drift and with a lower temperature. This cold population of magnetospheric ions originates from the slow tail of the initial magnetospheric ion distribution that overlaps in velocity space with the cold ionospheric ions. We suspect that the relative drift between the two ion populations excites a mild instability that both heats the ionospheric ions (see discussion below) and cools the lowest velocity magnetospheric ions, similar to that described in Schriver and Ashour-Abdalla (1990). A full analysis of this instability is beyond the scope of the current paper, but is identified as an area of future work in order to fully understand the exchange of energy and momentum between the magnetospheric and ionospheric species. Finally, back at the upper boundary, labeled "iv," magnetospheric ions have been both reflected via magnetic mirroring and reaccelerated upwards via field-aligned potentials to a net upwards velocity of ∼+100 km/s. Panel 2b shows the magnetospheric electron distributions, with a hot distribution injected at the upper boundary (red) and a cooler, less dense distribution that is able to penetrate to the lower exobase boundary (blue). The downward going magnetospheric electrons at the lower boundary, labeled, "i," have an asymmetric, partially extended tail to higher downwards velocities, indicative of downwards acceleration via field-aligned potentials. At maximum for this simulation, the magnetospheric electrons impact the exobase at velocities up to $\sim -5 \times 10^6$ m/s, equivalent to ∼70 eV.

The ionospheric ion velocity distributions are shown in panel 2c. A cold core ionospheric ion distribution, labeled "i," is the dominant feature of the distribution with some heating compared to the initial distribution. In addition to this cold core, the distribution also possesses a downwards tail, labeled "ii," of ionospheric ions with velocities ≥200 km/s downwards. This tail results from downwards acceleration by ambipolar electrostatic fields generated by the initial expansion of the magnetospheric species downwards into the domain (i.e., as the magnetospheric electrons initially outrun the magnetospheric protons). At the upper boundary of the simulation, labeled "iii," there exists a population of significantly heated, upward moving ionospheric ions with median velocities of ∼+80 km/s, representing ionospheric ion outflow. This outflowing population results from *both* polar-wind type outflow due to the escape of the lighter ionospheric electrons and field-aligned potentials induced by the penetration of magnetospheric plasma into the strong crustal cusp region. Finally, panel 2d shows the ionospheric electron distributions, which possesses a cold core, labeled "i," and a slightly extended tail of downwards velocities, labeled "ii," at the lower boundary. The downward going tail of electrons reflects the field-aligned potentials accelerating electrons downwards in the same manner as that seen in the magnetospheric electron distribution. At the upper boundary, only very minor fluxes of somewhat heated ionospheric electrons are present.

Figure 3a shows the total potential for all five cases as a function of altitude above the exobase. The total potentials demonstrate that upward pointing electric fields exist above ∼250 km for all cases including the 0 nT crustal field case due to polar-wind type outflow where the ionospheric electrons outrun the

ionospheric ions. The upward ambipolar potential observed even in the absence of crustal fields is higher than those observed in-situ (e.g., maximum potentials of −1.5 V; see Xu et al., 2018), which is most likely caused by the heated ionospheric electrons (see Figure 2d) that upwell at a greater rate. The ionospheric heating seen in the model results here is also higher than observed in-situ (e.g., Fowler et al., 2015), ultimately due to limitations on the maximum ionospheric density we can simulate with the PIC model (i.e., higher ionospheric densities are less susceptible to heating from precipitating magnetospheric electrons). Nevertheless, as this study focuses on the role of crustal fields in altering the ambipolar potential, this "background" potential can be subtracted off as discussed below. Note also that the decrease in potential from ∼250 to 0 km is due to recycling of magnetospheric particles at the lower boundary. In Figure 3b, we show the difference in potential between the 0 nT case and the four cases with crustal fields, respectively, in particular to highlight the contribution to field-aligned potentials that arise upon inclusion of the crustal magnetic fields, thereby separating that contribution from ambipolar expansion potentials. For all four cases with crustal magnetic fields, potential differences ≤∼200 km above the exobase are near zero and thus negligible. At altitudes above the exobase of ≥∼200 km, the potential difference in all four cases decline with total potential drops at the upper boundary ranging from −4 V in the $B_c = 20$ nT crustal field case to −17 V in the $B_c = 160$ nT case. The potential drops correspond to upward pointing electric fields generated by the charge separation of magnetospheric plasma within the crustal magnetic field cusp. This field-aligned potential accelerates electrons downwards and ions upwards, thereby contributing to ionospheric outflow from the nightside ionosphere.

In Figure 3c, we show the ionospheric ion velocity distributions at the upper boundary of the simulation for all five cases at the end of each simulation time period. In all cases, the ionospheric ion distributions can be described as upward drifting Maxwellians, with drift speeds ranging from 63 km/s ($B_c = 0$ nT) to 80 km/s ($B_c = 160$ nT). Note that for all cases, the median drift speeds are slightly higher than estimated from the total potential drops alone, which range from 52 km/s ($B_c = 0$ nT) to 67 km/s ($B_c = 160$ nT). This apparent excess in the ionospheric median velocity is due to filtering of the lower energy tail of ionospheric ion distribution by the ∼8 V downwards pointing potential seen below 200 km in panel 3a. One can also see overall increases in the velocity distributions for the two strongest crustal magnetic field cases, $B_c = 80$ nT and 160 nT. To further quantify this increase, we computed the total ionospheric ion flux for each of the five cases by integrating over the velocity distribution as, $\Gamma = \int_{-\infty}^{\infty} vf(v)dv$. As listed as an inset in Figure 3c, the total ionospheric ion flux relative to the $B_c = 0$ nT case increases from a minimum of 1.08 for the $B_c = 40$ nT case to 1.53 and 2.25 for the $B_c = 80$ nT and 160 nT cases, respectively. We do note that the 40 nT case has a slightly lower relative flux than the 20 nT case which does not fit the overall trend; however, we suspect that for the 20 and 40 nT cases, the effect of the crustal fields on the ionospheric outflow may not be so robust as to produce a clear and distinguishable trend. Nevertheless, what is clear from Figure 3c is that strong crustal field cusps, where "strong" here implies ≥∼80 nT at the exobase, stimulate excess ionospheric ion outflow from the nightside ionosphere.

4. Discussion and Conclusion

The first fully kinetic simulations of martian crustal magnetic cusps regions presented here have quantified the role that crustal field cusps play in generating quasi-static field-aligned potentials and stimulating increased ionospheric outflow from the nightside ionosphere. Summarizing broadly, these simulations show that field-aligned potentials in martian crustal cusp regions can be self-consistently and stably formed and in turn, that these field-aligned potentials stimulate ionospheric ion outflow in excess of that which occurs in unmagnetized regions due to polar-wind type ambipolar expansion (e.g., Ergun et al., 2016; Xu et al., 2018). The formation of the additional field-aligned potentials arises from differential penetration of magnetospheric ions and electrons into cusps regions, in analogy with similar processes that occur in Earth's polar region (e.g., Schriver, 1999) and in lunar crustal magnetic field cusps (e.g., Deca et al., 2016; Poppe et al., 2012; Saito et al., 2010). Due to the presence of additional electrostatic field-aligned potentials, the model in turn predicts increased ionospheric ion outflow, with the total escaping ion flux correlated with the strength of the crustal magnetic field. Given the broad extent of crustal magnetic fields across Mars and in particular, the large cusp regions within these field topologies (e.g., Brain et al., 2007; Mitchell et al., 2007; Weber et al., 2017, 2019; Xu et al., 2019), it is likely that cusp-mediated ion escape is an

important term in atmospheric ion loss at Mars. Additional studies that attempt to calculate the globally integrated additional ionospheric ion outflow from crustal magnetic cusp regions across the entire nightside of Mars are encouraged as future work.

The simulation results also develop downwards accelerated electrons due to the presence of field-aligned potentials, analogous to observations of such fluxes on the nightside of Mars within crustal cusps (e.g., Akbari et al., 2019; Brain et al., 2006; Halekas et al., 2008; Xu et al., 2020). Indeed, the self-consistent nature of electrostatic fields ensures that the presence of upwards accelerated ions must be accompanied by downwards accelerated electrons. Such downwards accelerated electrons have been associated with discrete auroral emissions from Mars (e.g., Bertaux et al., 2005; Gérard et al., 2015; Soret et al., 2016; Xu et al., 2020). Here, simulation results show electron precipitation into the martian nightside atmosphere up to energies of at least ~70 eV for both magnetospheric and ionospheric electrons. Such electron energies are sufficient to stimulate aurora (e.g., Gronoff et al., 2012; Shematovich et al., 2008) and thus, our results are consistent with auroral emission generated by both direct magnetospheric electron precipitation *and* by the heating and subsequent downwards acceleration of ionospheric electrons.

Building on these results, there remains a wealth of additional variables to explore including the magnetospheric plasma properties (e.g., density, flow speed, temperature), the ionospheric plasma properties (density, temperature), and crustal magnetic field profile (i.e., we have assumed a dipolar structure for this study, but that need not necessarily be the case (e.g., Brain et al., 2003)). Additionally, further simulations using this PIC model may also be straightforwardly altered such that ionospheric species are not preloaded into the simulation but rather generated according to the precipitating flux of suprathermal electrons (e.g., in the manner of Lillis et al., 2009). Given that precipitating suprathermal electrons are thought to be one of the dominant sources of the nightside martian ionosphere, especially in the deep nightside for solar zenith angles >~115° (e.g., Girazian et al., 2017a; Lillis et al., 2009, 2011, 2018), understanding the fully self-consistent manner in which the magnetospheric species interact with the crustal magnetic field cusp, associated field-aligned potentials, and stimulate ionization of martian neutrals is a natural next step.

Data Availability Statement

Model results are publicly available at https://doi.org/10.6078/D1BX2F.

Acknowledgments
The authors gratefully acknowledge support from NASA's Solar System Workings program, grant #NNX16AR94G.

References

Adams, D., Xu, S., Mitchell, D. L., Lillis, R. J., Fillingim, M., Andersson, L., et al. (2018). Using magnetic topology to probe the sources of Mars' nightside ionosphere. *Geophysical Research Letters*, *45*, 12190–12197. https://doi.org/10.1029/2018GL080629

Airapetian, V. S., Glocer, A., Khazanov, G. V., Loyd, R. O. P., France, K., Sojka, J., et al. (2017). How hospitable are space weather affected habitable zones? The role of ion escape. *The Astrophysical Journal Letters*, *836*, 1–5. https://doi.org/10.3847/2041-8213/836/1/L3

Akbari, H., Andersson, L., Fowler, C., & Mitchell, D. (2019). Spectral analysis of accelerated electron populations at Mars. *Journal of Geophysical Research: Space Physics*, *124*, 8056–8065. https://doi.org/10.1029/2019JA026738

André, M., & Yau, A. (1997). Theories and observations of ion energization and outflow in the high latitude magnetosphere. *Space Science Reviews*, *80*, 27–48.

Bertaux, J.-L., Leblanc, F., Witasse, O., Quémerais, E., Lilensten, J., Stern, S. A., et al. (2005). Discovery of aurora on Mars. *Nature*, *435*(7), 790–794.

Bibring, J.-P., Langevin, Y., Gendrin, A., Gondet, B., Poulet, F., Berthé, M., et al., and the OMEGA Team (2005). Mars surface diversity as revealed by the OMEGA/Mars Express observations. *Science*, *307*, 1576–1581.

Birdsall, C. K., & Langdon, A. B. (1985). *Plasma physics via computer simulation*. New York, NY: McGraw-Hill.

Bisikalo, D. V., Shematovich, V. I., Gérard, J.-C., & Hubert, B. (2017). Influence of the crustal magnetic field on the Mars aurora electron flux and UV brightness. *Icarus*, *282*, 127–135. https://doi.org/10.1016/j.icarus.2016.08.035

Brain, D. A., Bagenal, F., Acuña, M. H., & Connerney, J. E. P. (2003). martian magnetic morphology: Contributions from the solar wind and crust. *Journal of Geophysical Research*, *108*(A12), 1424. https://doi.org/10.1029/2002JA009482

Brain, D., Barabash, S., Boesswetter, A., Bougher, S., Brecht, S., Chanteur, G., et al. (2010). A comparison of global models for the solar wind interaction with Mars. *Icarus*, *206*, 139–151. https://doi.org/10.1016/j.icarus.2009.06.030

Brain, D. A., Halekas, J. S., Peticolas, L. M., Lin, R. P., Luhmann, J. G., Mitchell, D. L., et al. (2006). On the origin of aurorae on Mars. *Geophysical Research Letters*, *33*, L01201. https://doi.org/10.1029/2005GL024782

Brain, D. A., Lillis, R. J., Mitchell, D. L., Halekas, J. S., & Lin, R. P. (2007). Electron pitch angle distributions as indicators of magnetic field topology near Mars. *Journal of Geophysical Research*, *112*, A09201. https://doi.org/10.1029/2007JA012435

Brain, D. A., McFadden, J. P., Halekas, J. S., Connerney, J. E. P., Bougher, S. W., Curry, S., et al. (2015). The spatial distribution of planetary ion fluxes near Mars observed by MAVEN. *Geophysical Research Letters*, *42*, 9142–9148. https://doi.org/10.1002/2015GL065293

Brecht, S. H., & Ledvina, S. A. (2014). The role of the martian crustal magnetic fields in controlling ionospheric loss. *Geophysical Research Letters*, *41*, 5340–5346. https://doi.org/10.1002/2014GL060841

Brecht, S. H., Ledvina, S. A., & Bougher, S. W. (2016). Ionospheric loss from Mars as predicted by hybrid particle simulations. *Journal of Geophysical Research: Space Physics*, *121*, 10190–10208. https://doi.org/10.1002/2016JA022548

Carlsson, E., Fedorov, A., Barabash, S., Budnik, E., Grigoriev, A., Gunell, H., et al. (2006). Mass composition of the escaping plasma at Mars. *Icarus*, *182*, 320–328.

Collinson, G., Mitchell, D., Glocer, A., Grebowsky, J., Peterson, W. K., Connerney, J., et al. (2015). Electric Mars: The first direct measurement of an upper limit for the martian "polar wind" electric potential. *Geophysical Research Letters*, *42*, 9128–9134. https://doi.org/10.1002/2015GL065084

Cravens, T. E., Hoppe, A., & Ledvina, S. A. (2002). Pickup ions near Mars associated with escaping oxygen atoms. *Journal of Geophysical Research*, *107*(A8), 1170–1180. https://doi.org/10.1029/2001JA000125

Cui, J., Wu, X.-S., Gu, H., Jiang, F.-Y., & Wei, Y. (2019). Photochemical escape of atomic C and N on Mars: Clues from a multi-instrument MAVEN dataset. *Astronomy and Astrophysics*, *621*, A23. https://doi.org/10.1051/0004-6361/201833749

Davis, J. M., Balme, M., Grindrod, P. M., Williams, R. M. E., & Gupta, S. (2016). Extensive Noachian fluvial systems in Arabia Terra: Implications for early martian climate. *Geology*, *44*(10), 847–850. https://doi.org/10.1130/G38247.1

Deca, J., Divin, A., Wang, X., Lembège, B., Markidis, S., Horányi, M., & Lapenta, G. (2016). Three-dimensional full-kinetic simulation of the solar wind interactions with a vertical dipolar lunar magnetic anomaly. *Geophysical Research Letters*, *43*, 4136–4144. https://doi.org/10.1002/2016GL068535

Dong, C., Bougher, S., Ma, Y., Toth, G., Nagy, A., & Najib, D. (2014). Solar wind interaction with Mars upper atmosphere: Results from the one-way coupling between the multi-fluid MHD model and the MTGCM model. *Geophysical Research Letters*, *41*, 2708–2715. https://doi.org/10.1002/2014GL059515

Dong, Y., Fang, X., Brain, D. A., McFadden, J. P., Halekas, J. S., Connerney, J. E., et al. (2015). Strong plume fluxes at Mars observed by MAVEN: An important planetary ion escape channel. *Geophysical Research Letters*, *42*, 8942–8950. https://doi.org/10.1002/2015GL065346

Dong, C., Lee, Y., Ma, Y., Lingam, M., Bougher, S., Luhmann, J., et al. (2018). Modeling martian atmospheric losses over time: Implications for exoplanetary climate evolution and habitability. *The Astrophysical Journal Letters*, *859*, 1–5. https://doi.org/10.3847/2041-8213/aac489

Dong, C., Lingam, M., Ma, Y., & Cohen, O. (2017). Is proxima Centauri b habitable? A study of atmospheric loss. *The Astrophysical Journal Letters*, *837*, 1–6. https://doi.org/10.3847/2041-8213/aa6438

Dubinin, E., Chanteur, G., Fraenz, M., Modolo, R., Woch, J., Roussos, E., et al. (2008a). Asymmetry of plasma fluxes at Mars. ASPERA-3 observations and hybrid simulations. *Planetary and Space Science*, *56*, 832–835.

Dubinin, E., Chanteur, G., Fraenz, M., & Woch, J. (2008b). Field-aligned currents and parallel electric field potential drops at Mars. Scaling from the Earth' aurora. *Planetary and Space Science*, *56*, 868–872.

Dubinin, E., Fraenz, M., Fedorov, A., Lundin, R., Edberg, N., Duru, F., & Vaisberg, O. (2011). Ion energization and escape on Mars and Venus. *Space Science Reviews*, *162*, 173–211. https://doi.org/10.1007/s11214-011-9831-7

Dubinin, E., Fraenz, M., Pätzold, M., Woch, J., McFadden, J., Fan, K., et al. (2020). Impact of martian crustal magnetic field on the ion escape. *Journal of Geophysical Research: Space Physics*, *125*. 10574–10579. https://doi.org/10.1029/2020JA028010

Edwards, C. S., & Ehlmann, B. L. (2015). Carbon sequestration on Mars. *Geology*, *43*(10), 863–866.

Egan, H., Ma, Y., Dong, C., Modolo, R., Jarvinen, R., Bougher, S., et al. (2018). Comparison of global martian plasma models in the context of MAVEN observations. *Journal of Geophysical Research: Space Physics*, *123*, 3714–3726. https://doi.org/10.1029/2017JA025068

Ergun, R. E., Andersson, L. A., Fowler, C. M., Woodson, A. K., Weber, T. D., Delory, G. T., et al. (2016). Enhanced loss at Mars due to an ambipolar electric field from electron heating. *Journal of Geophysical Research: Space Physics*, *121*, 4668–4678. https://doi.org/10.1002/2016JA022349

Fang, X., Liemohn, M. W., Nagy, A. F., Luhmann, J. G., & Ma, Y. (2010). On the effect of the martian crustal magnetic field on atmospheric erosion. *Icarus*, *206*, 130–138.

Fang, X., Ma, Y., Brain, D., Dong, Y., & Lillis, R. (2015). Control of Mars global atmospheric loss by the continuous rotation of the crustal magnetic field: A time-dependent MHD study. *Journal of Geophysical Research: Space Physics*, *120*, 10926–10944. https://doi.org/10.1002/2015JA021605

Fowler, C. M., Andersson, L., Ergun, R. E., Morooka, M., Delory, G., Andrews, D. J., et al. (2015). The first in situ electron temperature and density measurements of the martian nightside ionosphere. *Geophysical Research Letters*, *42*, 8854–8861. https://doi.org/10.1002/2015GL065267

Fox, J. L., & Hać, A. B. (2009). Photochemical escape of oxygen from Mars: A comparison of the exobase approximation to a Monte Carlo method. *Icarus*, *204*, 527–544. https://doi.org/10.1016/j.icarus.2009.07.005

Gérard, J.-C., Soret, L., Libert, L., Lundin, R., Stiepen, A., Radioti, A., & Bertaux, J.-L. (2015). Concurrent observations of ultraviolet aurora and energetic electron precipitation with Mars Express. *Journal of Geophysical Research: Space Physics*, *120*, 6749–6765. https://doi.org/10.1002/2015JA021150

Girazian, Z., Mahaffy, P., Lillis, R. J., Benna, M., Elrod, M., Fowler, C. M., & Mitchell, D. L. (2017b). Ion densities in the nightside ionosphere of Mars: Effects of electron impact ionization. *Geophysical Research Letters*, *44*, 11248–11256. https://doi.org/10.1002/2017GL075431

Girazian, Z., Mahaffy, P. R., Lillis, R. J., Benna, M., Elrod, M., & Jakosky, B. M. (2017a). Nightside ionosphere of Mars: Composition, vertical structure, and variability. *Journal of Geophysical Research: Space Physics*, *122*, 4712–4725. https://doi.org/10.1002/2016JA023508

Gronoff, G., Wedlund, C. S., Mertens, C. J., Barthélemy, M., Lillis, R. J., & Witasse, O. (2012). Computing uncertainties in ionosphere-airglow models: II. The martian airglow. *Journal of Geophysical Research*, *117*, A05309. https://doi.org/10.1029/2011JA017308

Haider, S. A., Kim, J., Nagy, A. F., Keller, C. N., Verigin, M. I., Gringauz, K. I., et al. (1992). Calculated ionization rates, ion densities, and airglow emission rates due to precipitating electrons in the nightside ionosphere of Mars. *Journal of Geophysical Research*, *97*(A7), 10637–10641.

Haider, S. A., Pandya, B. M., & Molina-Cuberos, G. J. (2013). Nighttime ionosphere caused by meteoroid ablation and solar wind electron-proton-hydrogen impact on Mars: MEX observation and modeling. *Journal of Geophysical Research: Space Physics*, *118*, 6786–6794. https://doi.org/10.1002/jgra.50590

Halekas, J. S., Brain, D. A., Lin, R. P., Luhmann, J. G., & Mitchell, D. L. (2008). Distribution and variability of accelerated electrons at Mars. *Advances in Space Research*, *41*, 1347–1352. https://doi.org/10.1016/j.asr.2007.01.034

Harada, Y., Halekas, J. S., McFadden, J. P., Mitchell, D. L., Mazelle, C., Connerney, J. E. P., et al. (2015). Marsward and tailward ions in the near-Mars magnetotail: MAVEN observations. *Geophysical Research Letters*, *42*, 8925–8932. https://doi.org/10.1002/2015GL065005

Hess, S. L., Henry, R. M., & Tillman, J. E. (1979). The seasonal variation of atmospheric pressure on Mars as affected by the south polar cap. *Journal of Geophysical Research*, *84*(B6), 2923–2927.

Holmström, M., & Wang, X.-D. (2015). Mars as a comet: Solar wind interaction on a large scale. *Planetary and Space Science*, *119*, 43–47.

Jakosky, B. M., Brain, D., Chaffin, M., Curry, S., Deighan, J., Grebowsky, J., et al. (2018). Loss of the martian atmosphere to space: Present-day loss rates determined from MAVEN observations and integrated loss through time. *Icarus*, *315*, 146–157. https://doi.org/10.1016/j.icarus.2018.05.030

Jakosky, B. M., Pepin, R. O., Johnson, R. E., & Fox, J. L. (1994). Mars atmospheric loss and isotopic fractionation by solar-wind-induced sputtering and photochemical escape. *Icarus*, *111*, 271–288.

Jarvinen, R., Brain, D. A., & Luhmann, J. G. (2016). Dynamics of planetary ions in the induced magnetospheres of Venus and Mars. *Planetary and Space Science*, *127*, 1–14. https://doi.org/10.1016/j.pss.2015.08.012

Jarvinen, R., Brain, D. A., Modolo, R., Fedorov, A., & Holmström, M. (2018). Oxygen ion energization at Mars: Comparison of MAVEN and Mars express observations to global hybrid simulation. *Journal of Geophysical Research: Space Physics*, *123*, 1678–1689. https://doi.org/10.1002/2017JA024884

Leblanc, F., & Johnson, R. E. (2001). Sputtering of the martian atmosphere by solar wind pick-up ions. *Planetary and Space Science*, *49*, 645–656.

Leblanc, F., Witasse, O., Winningham, J., Brain, D., Lilensten, J., Blelly, P. L., et al. (2006). Origins of the martian aurora observed by spectroscopy for investigation of characteristics of the atmosphere of Mars (SPICAM) on board Mars express. *Journal of Geophysical Research*, *111*, A09313. https://doi.org/10.1029/2006JA011763

Ledvina, S. A., Brecht, S. H., Brain, D. A., & Jakosky, B. M. (2017). Ion escape rates from Mars: Results from hybrid simulations compared to MAVEN observations. *Journal of Geophysical Research: Space Physics*, *122*, 8391–8408. https://doi.org/10.1002/2016JA023521

Lillis, R. J., Deighan, J., Fox, J. L., Bougher, S. W., Lee, Y., Combi, M. R., et al. (2017). Photochemical escape of oxygen from Mars: First results from MAVEN in situ data. *Journal of Geophysical Research: Space Physics*, *122*, 3815–3836. https://doi.org/10.1002/2016JA023525

Lillis, R. J., Fillingim, M. O., & Brain, D. A. (2011). Three-dimensional structure of the martian nightside ionosphere: Predicted rates of impact ionization from Mars Global Surveyor magnetometer and electron reflectometer measurements of precipitating electrons. *Journal of Geophysical Research*, *116*, A12317. https://doi.org/10.1029/2011JA016982

Lillis, R. J., Fillingim, M. O., Peticolas, L. M., Brain, D. A., Lin, R. P., & Bougher, S. W. (2009). Nightside ionosphere of Mars: Modeling the effects of crustal magnetic fields and electron pitch angle distributions on electron impact ionization. *Journal of Geophysical Research*, *114*, E11009. https://doi.org/10.1029/2009JE003379

Lillis, R. J., Mitchell, D. L., Steckiewicz, M., Brain, D., Xu, S., Weber, T., et al. (2018). Ionizing electrons on the martian nightside: Structure and variability. *Journal of Geophysical Research: Space Physics*, *123*, 4349–4363. https://doi.org/10.1029/2017JA025151

Luhmann, J. G., Johnson, R. E., & Zhang, M. H. G. (1992). Evolutionary impact of sputtering the martian atmosphere by O^+ pickup ions. *Geophysical Research Letters*, *19*(21), 2151–2154.

Lundin, R., Winningham, D., Barabash, S., Frahm, R., Holmström, M., Sauvaud, J.-A., et al. (2006a). Plasma acceleration above martian magnetic anomalies. *Science*, *311*(5763). 980–983. https://doi.org/10.1126/science.1122071

Lundin, R., Winningham, D., Barabash, S., Frahm, R., Brain, D., Nilsson, H., et al. (2006b). Auroral plasma acceleration above martian magnetic anomalies. *Space Science Reviews*, *126*(1), 333–354. https://doi.org/10.1007/s11214-006-9086-x

Ma, Y., Nagy, A., Sokolov, I. V., & Hansen, K. C. (2004). Three-dimensional, multispecies, high spatial resolution MHD studies of the solar wind interaction with Mars. *Journal of Geophysical Research*, *109*, A07211. https://doi.org/10.1029/2003JA010367

Mitchell, D. L., Lillis, R. J., Lin, R. P., Connerney, J. E. P., & Acuña, M. H. (2007). A global map of Mars' crustal magnetic field based on electron reflectometry. *Journal of Geophysical Research*, *112*, E01002. https://doi.org/10.1029/2005JE002564

Nimmo, F., & Gilmore, M. S. (2001). Constraints on the depth of magnetized crust on Mars from impact craters. *Journal of Geophysical Research*, *106*(E6), 12315–12323.

Němec, F., Morgan, D. D., Gurnett, D. A., & Brain, D. A. (2011). Areas of enhanced ionization in the deep nightside ionosphere of Mars. *Journal of Geophysical Research*, *116*, E06006. https://doi.org/10.1029/2011JE003804

Owen, T. (1992). The composition and early history of the atmosphere of Mars. In H. H. Kieffer, B. M. Jakosky, C. W. Snyder, & M. S. Matthews (Eds.), *Mars* (pp. 818–834). Tucson, AZ: University of Arizona Press. https://doi.org/10.2307/j.ctt207g59v

Poppe, A. R., Halekas, J. S., Delory, G. T., & Farrell, W. M. (2012). Particle-in-cell simulations of the solar wind interactions with lunar crustal magnetic anomalies: Magnetic cusp regions. *Journal of Geophysical Research*, *117*, A09105. https://doi.org/10.1029/2012JA017844

Poulet, F., Bibring, J.-P., Mustard, J. F., Gendrin, A., Mangold, N., Langevin, Y., et al. (2005). Phyllosilicates on mars and implications for early martian climate. *Nature*, *438*(7068), 623–627. https://doi.org/10.1038/nature04274

Reiff, P. H., Collin, H. L., Craven, J. D., Burch, J. L., Winningham, J. D., Shelley, E. G., et al. (1988). Determination of auroral electrostatic potentials using high- and low-altitude particle distributions. *Journal of Geophysical Research*, *93*(A7), 7441–7465.

Romanelli, N., Modolo, R., Leblanc, F., Chaufray, J.-Y., Hess, S., Brain, D., et al. (2018). Effects of the crustal magnetic fields and changes in the IMF orientation on the magnetosphere of Mars: MAVEN observations and LatHyS results. *Journal of Geophysical Research: Space Physics*, *123*, 5315–5333. https://doi.org/10.1029/2017JA025155

Safaeinili, A., Kofman, W., Mouginot, J., Gim, Y., Herique, A., Ivanov, A. B., et al. (2007). Estimation of the total electron content of the martian ionosphere using radar sounder surface echoes. *Geophysical Research Letters*, *34*, L23204. https://doi.org/10.1029/2007GL032154

Saito, Y., Asamura, K., Tanaka, T., Nishino, M. N., Yamamoto, T., Terakawa, Y., et al. (2010). In-flight performance and initial results of plasma energy angle and composition experiment (PACE) on SELENE (kaguya). *Space Science Reviews*, *154*, 265–303.

Schriver, D. (1999). Particle simulation of the auroral zone showing parallel electric fields, waves, and plasma acceleration. *Journal of Geophysical Research*, *104*(A7), 14655–14670.

Schriver, D., & Ashour-Abdalla, M. (1990). Cold plasma heating in the plasma sheet boundary layer: Theory and simulations. *Journal of Geophysical Research*, *95*(A4), 3987–4005.

Schriver, D., & Ashour-Abdalla, M. (1993). Self-consistent formation of parallel electric fields in the auroral zone. *Geophysical Research Letters*, *20*(6), 475–478.

Seager, S. (2013). Exoplanet habitability. *Science*, *340*, 577–581. https://doi.org/10.1126/science.1232226

Shematovich, V. I., Bisikalo, D. V., Gérard, J.-C., Cox, C., Bougher, S. W., & Leblanc, F. (2008). Monte Carlo model of electron transport for the calculation of Mars dayglow emissions. *Journal of Geophysical Research*, *113*, E02011. https://doi.org/10.1029/2007JE002938

Soret, L., Gérard, J.-C., Libert, L., Shematovich, V. I., Bisikalo, D. V., Stiepen, A., & Bertaux, J.-L. (2016). SPICAM observations and modeling of Mars aurorae. *Icarus*, *264*, 398–406.

Tian, F., Kasting, J. F., & Solomon, S. C. (2009). Thermal escape of carbon from the early martian atmosphere. *Geophysical Research Letters*, *36*, L02205. https://doi.org/10.1029/2008GL036513

Voorhies, C. V. (2008). Thickness of the magnetic crust of Mars. *Journal of Geophysical Research*, *113*, E04004. https://doi.org/10.1029/2007JE002928

Walterscheid, R. L., Hickey, M. P., & Schubert, G. (2013). Wave heating and Jeans escape in the martian upper atmosphere. *Journal of Geophysical Research: Planets*, *118*, 2413–2422. https://doi.org/10.1002/jgre.20164

Weber, T., Brain, D., Mitchell, D., Xu, S., Connerney, J., & Halekas, J. (2017). Characterization of low-altitude nightside martian magnetic topology using electron pitch angle distributions. *Journal of Geophysical Research: Space Physics*, *122*, 9777–9789. https://doi.org/10.1002/2017JA024491

Weber, T., Brain, D., Mitchell, D., Xu, S., Espley, J., Halekas, J., et al. (2019). The influence of solar wind pressure on martian crustal magnetic field topology. *Geophysical Research Letters*, *46*, 2347–2354. https://doi.org/10.1029/2019GL081913

Withers, P., Mendillo, M., Hinson, D. P., & Cahoy, K. (2008). Physical characteristics and occurrence rates of meteoric plasma layers detected in the martian ionosphere by the Mars Global Surveyor Radio Science Experiment. *Journal of Geophysical Research*, *113*, A12314. https://doi.org/10.1029/2008JA013636

Wu, X.-S., Cui, J., Xu, S. S., Lillis, R. J., Yelle, R. V., Edberg, N. J. T., et al. (2019). The morphology of the topside martian ionosphere: Implications on bulk ion flow. *Journal of Geophysical Research: Planets*, *124*, 734–751. https://doi.org/10.1029/2018JE005895

Xu, S., Mitchell, D. L., McFadden, J. P., Collinson, G., Harada, Y., Lillis, R., et al. (2018). Field-aligned potentials at Mars from MAVEN observations. *Geophysical Research Letters*, *45*, 10119–10127. https://doi.org/10.1029/2018GL080136

Xu, S., Mitchell, D. L., McFadden, J. P., Fillingim, M. O., Andersson, L., Brain, D. A., et al. (2020). Inverted-V electron acceleration events concurring with localized auroral observations at Mars with MAVEN. *Geophysical Research Letters*, *47*, e2020GL087414. https://doi.org/10.1029/2020GL087414

Xu, S., Weber, T., Mitchell, D. L., Brain, D. A., Mazelle, C., DiBraccio, G. A., & Espley, J. (2019). A technique to infer magnetic topology at Mars and its application to the terminator region. *Journal of Geophysical Research: Space Physics*, *124*, 1823–1842. https://doi.org/10.1029/2018JA026366